Cement and Concrete Research 42 (2012) 194–204

Contents lists available at SciVerse ScienceDirect

Cement and Concrete Research

journal homepage: http://ees.elsevier.com/CEMCON/default.asp

Pore structure characterization of cement pastes blended with high-volume fly-ash

Qiang Zeng [a,b], Kefei Li [a,*], Teddy Fen-chong [b], Patrick Dangla [b]

[a] Civil Engineering Department, Tsinghua University, Beijing, 100084, PR China
[b] Université Paris-EST, Laboratoire Navier CNRS, 77420, Champs-sur-Marne, France

ARTICLE INFO

Article history:
Received 14 January 2011
Accepted 23 September 2011

Keywords:
Characterization (B)
Pore size distribution (B)
Surface area (B)
Fly ash (D)

ABSTRACT

The pore structure of cement pastes incorporating fly-ash was evaluated during their hydration process through gravimetry method, mercury intrusion porosimetry (MIP) and nitrogen adsorption/desorption (NAD) methods. The pore structure of samples is characterized by the total porosity, pore size distribution (PSD), pore internal surface area as well as characteristic pore sizes. The correlation between the hydration process and the formed pore structure is investigated. The results indicate that: (i) w/b ratios have determinant impact on all characteristics of pore structure; (ii) fly-ash replacement ratio can influence the pore structure significantly at early age but this influence becomes less important with sample age by fly-ash hydration process; (iii) the total porosity and specific surface area are well correlated with the chemical kinetics of hydration through hydration degree or the formed gel/space ratio but the critical pore size is rather independent on the chemical kinetics.

1. Introduction

Fly-ash, an industrial by-product in powder form with a granulometry of 0.5–100 μm, is widely used as a supplementary cementitious material (SCM) for Portland cements. As properly used, fly-ash can help cement-based materials to gain good workability, mechanical properties as well as durability [1,2]. The fly-ash particles, much less reactive than cement grains, can accelerate the cement hydration kinetics by heterogeneous nucleation effect [3] and surface absorption effect [4]. Moreover, by their spherical geometry, the fly-ash particles can act as "ball-bearing" to better the rheological properties of fresh pastes [5,6]. The hydration process of fly-ash particles, known as pozzolana reaction, is much slower compared to cement grains and these particles continue to react with pore solution and cement hydrates for years after the hardening of pastes [5–8]. Accordingly, the microstructure of hardened cement pastes evolves substantially with the continuous formation of pozzolana reaction products, C–S–H gel in cement chemistry terms, in the pore space enclosed by cement hydrates.

As typical porous media, cement pastes adopt a pore structure with broad pore size distribution from nanometer to micrometer scales [9]. Moreover, the connectivity of the pores of different sizes seems to be complicated and "ink-bottle" geometry exists extensively in the pore network [10]. Nowadays, no experimental method allows to measure the pore structure of cement pastes completely. So far, numerous experimental methods have been developed to measure or assess the pore structure, and the most widely used methods include the mercury intrusion porosimetry (MIP) and nitrogen adsorption/desorption (NAD) methods. The MIP measurement remains still the preferred method for pore structure evaluation due to its large range of pore size measurement and easy operation [11], although the measurement loses its accuracy for "ink-bottle" pores and fractures can be possibly induced in samples under high intrusion pressure [10,12]. The gas adsorption method has also been used to identify the pore structure of cement-based materials for decades [13–16]. On the basis of the adsorbed gas quantity, the internal surface area of pores can be evaluated from the Langmuir monomolecular layer theory or the BET multilayer adsorption theory. Furthermore, the pore size distribution can be obtained using Barrett–Joyner–Halenda (BJH) interpretation based on capillary condensation [13]. Note that the desorption phase of NAD is similar to the intrusion phase of MIP from the point of view of nonwetting phase propagation in pores [17]. Thus the pore size distributions obtained from NAD and MIP measurements can be compared for the mutual range of pore size. Actually, the combination of MIP and NAD for pore structure characterization has been widely used in such fields as industry catalyst [17], soil engineering [18] and artificial materials [19]. Recent works by Kaufmann et al. [20] and Kaufmann [21] showed the application of NAD, MIP and other methods combined together to evaluate the pore structure of cement-based materials.

Compared to the extensive results available on hydration mechanisms, microstructure and mechanical properties of high-volume fly-ash cement pastes, relatively few investigations are dedicated to the relation between the hydration process and the evolution of pore structure characteristics. In this paper, systematic experiments were firstly performed on the pore structure of high-volume fly-ash cement composites. Different pretreatment methods of samples

---

* Corresponding author. Tel./fax: +86 10 6278 1408.
E-mail address: likefei@tsinghua.edu.cn (K. Li).

0008-8846/$ – see front matter © 2011 Elsevier Ltd. All rights reserved.
doi:10.1016/j.cemconres.2011.09.012

were adopted to obtain reliable measurement of pore structure. The NAD and MIP were used as complementary methods to evaluate the porosity, pore size distribution and characteristic pore sizes. Then, the hydration kinetics is quantified for the cement pastes to investigate the relation between hydration process and the pore structure evolution. Finally, the nanostructure of the hydrate, C–S–H, is recalled to interpret the experimental observations and to understand the pore structure evolution.

2. Materials and experiments

2.1. Materials

A low-calcium fly-ash and an ordinary Portland cement were used in this study. The chemical composition and physical properties of cement and fly-ash are given in Table 1. The mineral contents of cement were analyzed, through Bogue's procedure [22], as C_2S (21.38%), C_3S (58.88%), C_3A (6.49%), C_4AF (8.77%), gypsum (0.75%) and others (3.73%).

2.2. Sample preparation

Cement paste samples were prepared with two water to binder (w/b) ratios (0.3, 0.5), and four fly-ash contents. The fly-ash content, f_f, is noted as the mass ratio between fly-ash and binder (fly-ash and cement). The detailed mixture is given in Table 2. After mixing, cement pastes of different mixtures were cast into cylinder tubes of 10 mm diameter and placed in room condition with temperature controlled at 20 °C. After that, the hardened specimens were demoulded from the tubes at the age of 3 d, then immersed into water. To avoid the possible leaching, the ratio of specimen to water is kept at roughly 1:1 in volume or 2:1 in weight. At the ages of 7 d, 28 d and 90 d, specimens were taken out of water and crushed to particle samples of size 1 mm–2 mm for later experiments. The crushed particles were selected deliberately from the middle part of cylinder specimens to avoid the inhomogeneity of material. The crushed samples were then vacuum-dried immediately to stop the hydration and control the possible carbonation extent as low as possible.

The subsequent experiments and their respective sample treatment procedures are summarized in Table 3. The procedure of sample preparation was adapted for different experiments. For MIP and NAD tests, the samples were subjected to drying procedure by freezing (F-drying). For porosity evaluation by gravimetry method, the samples, each 1–1.5 g, were firstly vacuum-saturated by liquid water and then immersed both in methanol and acetone of 100 ml. The solvent (methanol or acetone) was renewed every hour during the first 24 h, and every 24 h afterwards for 7 d. The samples were then oven-dried at 50 °C for 24 h. Before and after oven-dry procedure the weight of samples was measured to the accuracy to 0.001 g. Note that the solvent may alter the microstructure of cement-based materials [23,24], this drying technique is retained in this study just for comparison of porosity measurement. For helium pycnometry, selective dissolution and TGA experiments, the samples were firstly vacuum-saturated by liquid water and then oven-dried at 105 ± 1 °C for 24 h. The dried samples were ground to powder, having the 80 μm-sieve passing ratio of 95%.

Table 1
Chemical composition and physical properties of cement and fly-ash.

Chemical composition/physical properties	Cement	Fly-ash
Silica (SiO_2, %)	22.93	57.60
Alumina (Al_2O_3, %)	4.29	21.90
Iron oxide (Fe_2O_3, %)	2.89	2.70
Calcium oxide (CaO, %)	66.23	7.80
Magnesium oxide (MgO, %)	1.92	1.68
Sulfur trioxide (SO3, %)	0.35	0.41
Sodium oxide (Na_2O(eq), %)	0.70	1.05
Free calcium oxide (CaO(f), %)	0.64	–
Chloride (Cl, %)	0.006	–
Loss on ignition (LOI, %)	1.70	7.05
Density (g/ml)	3.12	2.06
Specific area (m^2/kg)	343	355

Table 2
Mixture composition for cement pastes.

Paste	w/b (−)	Sample	Cement (kg/m^3)	Fly-ash (kg/m^3)	Water (kg/m^3)	f_f (−)
Paste I	0.5	PI0	1218	0	609	0%
		PIF1	937	234	588	20%
		PIF2	677	451	559	40%
		PIF3	435	650	543	60%
Paste II	0.3	PII0	1612	0	484	0%
		PIIF1	1224	306	459	20%
		PIIF2	874	583	437	40%
		PIIF3	556	834	417	60%

2.3. Determination of pore structure

2.3.1. Gravimetry

The principle of evaluating porosity by gravimetry is that the pore space occupied by a liquid can be determined via pore liquid evaporation or pore liquid replacement by another liquid. The sample saturated with a known liquid is weighted as m_s, after the oven-drying (105 ± 1 °C for 24 h) and solvent exchange procedures the sample is weighted as m_0 and m_d respectively. The porosity, therefore, can be calculated as,

$$\phi = \frac{(m_s - m_d)/(\rho_o - \rho_r)}{(m_s - m_d)/(\rho_o - \rho_r) + m_0/\rho_s} \tag{1}$$

where ρ_s is the density of solid skeleton, ρ_o is the density of the initial pore liquid phase and ρ_r is the density of phase occupying the pore spaces after drying or liquid exchange. For samples after oven-drying, ρ_r is the density of air, $\rho_r = 1.2041 \times 10^{-3}$ g/ml at 20 °C, which is negligible compared to liquid water density, $\rho_o = 0.997$ g/ml at 20 °C with $m_d = m_0$. For samples after solvent exchange, ρ_r are the densities of methanol and acetone, 0.7918 g/ml and 0.7925 g/ml at 20 °C respectively. The skeleton density ρ_s was determined by helium pycnometry and MIP, given in Table 4.

2.3.2. Mercury intrusion porosimetry

Mercury intrusion porosimetry is based on the principle that the intrusion volume of mercury into a porous medium depends on the applied pressure. If the pore geometry is assumed to be cylindrical,

Table 3
Experiments and sample preparation methods.

Experiment	Sample treatment	Measurement
MIP, NAD	Freezing-dry in liquid nitrogen (−196 °C) and vacuumed for 24 h	Porosity, pore size distribution, critical pore size, specific surface
MIP	Freezing-dry in liquid nitrogen (−196 °C) and vacuumed for 24 h	Skeleton density
Gravimetry	Water saturated, solvent exchange in methanol and acetone for 7 d, oven-dry at 50 °C for 24 h	Porosity
Helium pycnometry	Water saturated, oven-dry at 105 °C for 24 h, ground to powder $d_{95\%} = 80 \mu m$	Skeleton density
Selective dissolution	Water saturated, oven-dry at 105 °C for 24 h, ground to powder $d_{95\%} = 80 \mu m$	Fly-ash reaction degree
TGA	Water saturated, oven-dry at 105 °C for 24 h, ground to powder $d_{95\%} = 80 \mu m$	Non-evaporable water, $Ca(OH)_2$ content

Table 4
Skeleton density of porous cement pastes at different ages (g/cm^3).

Sample	Helium pycnometry			MIP		
	7 d	28 d	90 d	7 d	28 d	90 d
PI0	2.355	2.251	2.110	3.092	2.025	2.110
PIF1	2.298	2.223	2.182	2.394	2.068	2.055
PIF2	2.308	2.191	2.189	2.389	2.312	2.094
PIF3	2.286	2.210	2.219	2.375	2.109	2.315
PII0	2.383	2.410	2.347	2.647	2.254	2.191
PIIF1	2.320	2.338	2.282	2.276	2.232	2.168
PIIF2	2.391	2.314	2.297	2.255	2.060	2.067
PIIF3	2.494	2.322	2.340	2.284	1.820	2.148

the pore diameter (size) d can be related to the applied pressure P using Washburn equation [25],

$$d = -\frac{4\gamma cos\theta}{P} \tag{2}$$

where γ is the surface tension of mercury (0.485 N/m), and θ is the contact angle between mercury and pore wall (130°). A volume-weighted pore size distribution can be obtained by associating the intruded mercury volume at a given pressure with the pore size evaluated from Eq. (2). Note that the above assumption of straight cylindrical pores can lead to inaccurate interpretation for pore structure if "ink-bottle" pores exist. This point is to be discussed later in the paper. The mercury intrusion porosimetry used in this study is of type Autopore IV 9510 with maximum and minimum applied pressures as 414 MPa and 1.4 kPa, corresponding to a minimum pore size of 3 nm and maximum pore size of 800 μm.

2.3.3. Nitrogen adsorption/desorption

As a dried porous medium is put into a gas (nitrogen) environment, the internal surface of pores can adsorb a certain quantity of gas (nitrogen) molecules. The NAD experiment records the nitrogen gas pressure and the adsorbed nitrogen quantity, providing an adsorption isotherm. These data need further interpretation to deduce the pore structure of the porous medium. As the gas pressure is relatively low, it can be assumed that surface adsorption dominates. The Langmuir and BET approaches are most used to deduce the internal specific area of pores, based on monomolecular adsorption and multimolecular adsorption assumptions respectively. As the gas pressure goes on, condensation of nitrogen happens in small pores. The Barrett–Joyner–Halenda (BJH) interpretation uses pore condensation principle to evaluate the pore size distribution from the adsorption isotherm [13]. The relation between capillary condensation pressure and pore size d can be described by Kelvin equation. The detailed mathematical equations of the above interpretations can be referred to Ref. [26].

Note that the BJH estimation holds just for a relatively small range of pore size, $d \leq 60$ nm, since the pore condensation cannot happen for larger pores [26,27]. Also from BJH interpretation of adsorption isotherm the pore specific area is evaluated through pore condensation volume and the average pore size with cylindrical pore geometry assumption. The nitrogen adsorption/desorption on powder samples was carried out by a NAD device of type ASAP2010 with the nitrogen pressure range up to 126.66 kPa. Note that the relative pressure P/P_0 range for Langmuir/BET evaluation is 0.05–0.35 while that for BJH evaluation is 0.4–0.967 [26].

2.4. Evaluation of hydration degree

The cement chemistry defines the hydration degree as the mass ratio between the hydrated cement and the total cement. For pure cement this hydration degree can be evaluated by the quantity of non-evaporable water W_n^c, chemically bound to the hydrates, contained in the hardened cement paste [28]. As pozzolana additives like fly-ash are blended into cement, the hydration of fly-ash through pozzolanic reaction can also provide non-evaporable water. Thus quantifying the hydration process of fly-ash cement should identify respectively the hydration degree of fly-ash and that of cement. In this study, the selective dissolution method was used to evaluate the pozzolanic reaction degree of fly-ash. The principle of this method is that, except the unreacted fly-ash and undissolved minerals in unhydrated cement clinker, all hydration products are acid soluble [6,29]. Once the acid-solubility is determined for fly-ash and cement clinker the reaction degree of fly-ash can be expressed as,

$$\alpha_f = 1 - \frac{R_p - R_c f_c}{R_f f_f} \tag{3}$$

where, $f_{c,f}$ are the mass fractions of cement and fly-ash in binder, R_p is the residue (mass fraction) of ignited fly-ash paste after acid dissolution, R_c is the cement residue after acid dissolution ($R_c = 0.92\%$), R_f the residue of fly-ash after dissolution ($R_f = 92.88\%$). The mass conservation of total non-evaporable water in fly-ash pastes requires,

$$W_n^t = W_n^f + W_n^c = W_n^f \alpha_f \cdot f_f + W_n^c \alpha_c \cdot f_c \tag{4}$$

where α_c represents the hydration degree of cement, $W_n^{f,c}$ stand for the non-evaporable water quantity for unit mass of fly-ash and cement for a total hydration, $\alpha_{f,c} = 1.0$. In this study, these two values are retained as $W_n^f = 0.167$ [30] and $W_n^c = 0.23$ [28]. Then, the total hydration degree for blended pastes, α_t, and that of cement, α_c, can be evaluated as,

$$\alpha_t = \frac{W_n^t}{W_n^f \cdot f_f + W_n^c \cdot f_c} \quad \text{and} \quad \alpha_c = \frac{W_n^t - W_n^f}{W_n^c \cdot f_c} \tag{5}$$

In addition to the hydration degrees, the gel/space ratio β, defined as the volumetric fraction of formed gel (main hydration products) in hardened paste, is also used to characterize the pore structure formation process of fly-ash pastes. The gel/space ratio can be estimated as [6],

$$\beta = \frac{V_c \alpha_c f_c + V_f \alpha_f f_f}{f_c/\rho_c + f_f/\rho_f + (w/b)/\rho_w} \tag{6}$$

where $\rho_{c,f,w}$ stand for the density for cement, fly-ash and water, and $V_{c,f}$ are the formed gel volume by unit mass of cement and fly-ash, retained as $V_{c,f} = 2.06, 2.52$ according to Lam et al. [6].

3. Pore structure of high-volume fly-ash pastes

3.1. Porosity

The porosity of fly-ash cement pastes at different ages was determined by MIP and gravimetry and all results are illustrated in Fig. 1. From the figure, the first observation is that the w/b ratio has determinant influence on the porosity for Paste I (w/b = 0.5) and Paste II (w/b = 0.3). Then the porosity evolves with the curing age, reflecting the solid skeleton formation process from hydration reactions with time. For a certain age (7 d, 28 d or 90 d) and a given paste (I or II), the porosity is not strictly correlated to the fly-ash content f_f. The second observation is that, compared to the paste samples with $f_f = 0, 20\%$, the high-volume fly-ash pastes ($f_f = 40\%, 60\%$) maintain their total porosity from 7 d to 90 d. This observation reveals, for high-volume fly-ash cement pastes, that the hydration of fly-ash particles, consuming formed cement hydrates and producing their own hydrates, keeps the material porosity roughly at the same value with the hardening age. But it will be seen later that the pore size distribution changes substantially with the age. Further discussion on involved mechanisms is given later.

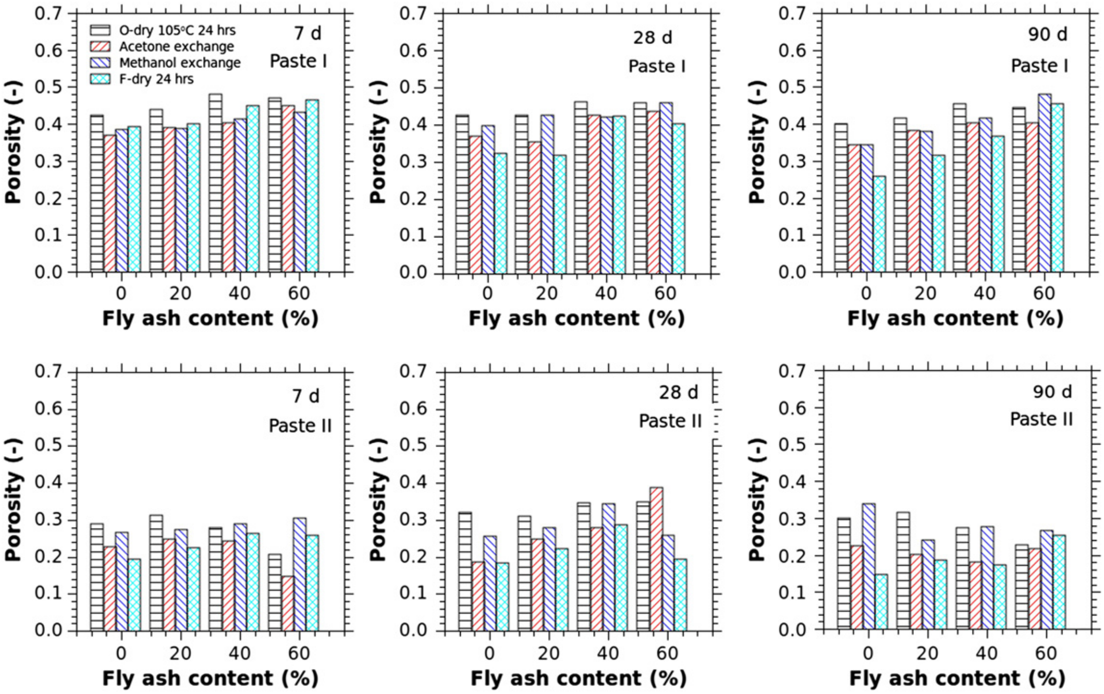

Fig. 1. Porosity of blended cement pastes with w/b = 0.5 (top) and those with w/b = 0.3 (bottom) at ages of 7 d, 28 d and 90 d (O-drying, acetone/methanol exchange by gravimetry and F-drying by MIP measurement).

In the figure are presented parallelly the porosity results from different sample pre-treatment procedures: F-drying (MIP), solvent exchange by acetone and methanol, and oven-drying (O-drying) at 105 °C. For Paste I (w/b = 0.5) samples with larger porosity, the porosity values from different methods have good agreement while notable difference is observed for porosity values for Paste II with smaller porosity. Besides the inherent heterogeneity of pore structure, the dispersion is due to the specific effect of each treatment to drive out the pore water. The oven-drying at 105 °C is proved more efficient thus larger porosity is obtained by this treatment for all cases while F-drying surely leaves some unfrozen water in very tiny pores (~nm) and the porosity adopts smaller values in almost all cases. The solvent exchange treatment, by acetone and methanol, gives porosity values between O-drying and F-drying, and larger porosity is observed by methanol exchange than acetone. This can be due to the smaller molecule size of methanol (molar volume 40.46 ml/mol) than acetone (molar volume 73.28 ml/mol), and methanol molecules can penetrate into layered structure of C–S–H gels [31].

3.2. Pore size distribution

The pore distribution was measured by MIP method and both cumulative pore size distribution (CPSD) and differential pore size distribution (DPSD) are presented in Fig. 2 for Paste I and Paste II. Note that the pore size measured by MIP refers to percolation size of pores (size of pore neck) corresponding to the intruded pressure rather than a real diameter of cylinder tubes. This size notion is different from the real geometry size of pores, e.g. observed directly from SEM or optical microscopy [10], thus should be interpreted only in the context of mercury intrusion. These percolation sizes and their distributions are used to investigate the evolution of pore structure of paste samples. In this paper the term “pore size” refers to percolation size of interconnected pore structure without special mention.

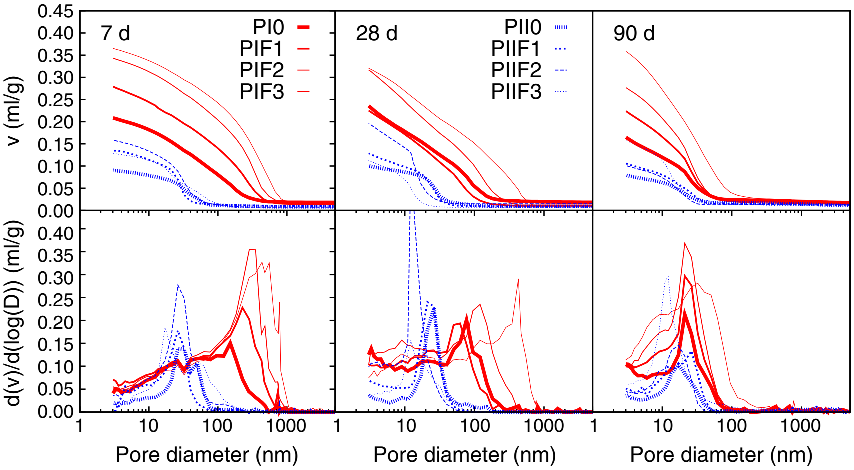

Fig. 2. Cumulative pore size distribution (top) and differential pore size distribution (bottom) of fly-ash cement pastes measured by MIP at different ages.

With higher w/b, Paste I samples have systematic higher CPSD than Paste II samples but the difference is narrowed with curing age by the secondary hydration of fly-ash and the subsequent filling effect of fly-ash hydration products in the formed pore structure. This effect can also be observed on the DPSD curves presented on the lower half of figure. In order to gain more insight into the pore size distribution with curing time and fly-ash content, the measured pore distribution is divided into four size ranges: gel micropores (<4.5 nm), meso-pores (4.5–50 nm), middle capillary pores (50–100\nm) and large capillary pores (>100 nm), according to Metha and Monteirio [9].

The pore size classification is presented in Figs. 3 and 4 for Pastes I and II. For Paste I (w/b = 0.5), the dominant ranges are the meso-pores and large capillary pores. With the curing age, the pore percolation size is decreased substantially and the meso-pores become the only dominant pore range, representing 80% pore fraction at 90 d. For Paste II (w/b = 0.3), the total porosity is decreased with curing age also by fly-ash secondary hydration but the relative fraction of pore ranges does not change significantly. The meso-pore range is also the dominant pore range for all cases. In terms of capillary pores (>50 nm), all samples, except PIF3, tend to have smaller capillary pore fraction with increase of fly-ash content f_f. A close study of the local w/c ratios of all pastes in Table 2 reveals that PIF3 has the largest w/c ratio (w/c = 1.25). Accordingly, this too large w/c ratio leaves capillary pores between cement hydrates too important to be filled by the later fly-ash hydration. It seems that the local w/c = 1.0 can be a good index for capillary porosity control in a cement–fly-ash–water system.

Now we focus on the micro-pore and meso-pore ranges. As aforementioned, the pore range measured by NAD is from nanometers to tens of nanometers. Therefore NAD can provide another information source for micro and meso-pores. The CPSD evaluated by the desorption branch of NAD, through BJH interpretation, is presented in Fig. 5. The CPSD curves show no significant difference for Pastes I and II at 7 d, then Paste I and II groups evolve with age and separate from each other. For Paste I group (w/b = 0.5), the adsorption volume increases with age, by 60% at 90 d while the volume augments just slightly for Paste II, i.e. around 20% at 90 d. This observation is actually due to the more advanced hydration degree of cement and fly-ash with higher w/b (more water), and deepened quantification is presented later.

3.3. Specific surface area

The specific surface area measured by NAD method is presented in Fig. 6 with Langmuir, BET and BJH interpretations. The specific surface area is closely related to the hydrate formation by cement or fly-ash. At early age of paste hardening, the hydrates are mainly due to cement grains, thus both cement hydration degree and cement quantity count for the specific surface area of a given paste. For pastes with high fly-ash content (PIF3, PIIF3), the cement quantity is less but cement hydration degree is higher. These two aspects interplay and give the specific surface values in terms of f_f in Fig. 6 for age of 7 d. With curing age, the fly-ash hydration contributes substantially to the specific surface area, as indicated in Fig. 6 for later age of 90 d. An almost linear relation is observed for specific surface value and fly-ash content at this age.

Fig. 6 shows also the dispersion of surface area values from different approaches. Due to its monolayer assumption, Langmuir approach gives larger area values than BET approach. Theoretically, the BJH interpretation gives just the specific surface for pores up to 60 nm, thus should be inferior to Langmuir and BET values. But Fig. 6 shows BJH values always higher than BET values, in some case even higher than Langmuir values. Similar observation has been reported [32]. The underlying reason is the cylindrical pore assumption of BJH interpretation, i.e. the specific surface is evaluated from the ratio between the condensation volume and the average pore radius [13]. This assumption can greatly underestimate the average pore radius as “ink-bottle” pores exist extensively in pore structure, which leads to a larger surface estimation than real surface. In other words, as the pore structure contains extensively “ink-bottle” pores at micro and mesopore scales, BJH method tends to overestimate the specific surface, as for Pastes I and II samples at later ages (28 d, 90 d) in Fig. 6.

3.4. Characterization of pore size

From the MIP measurement, we analyzed the pore size distribution by several characteristic pore sizes (radii), including critical pore radius, median pore radius as well as average pore radius. As aforementioned, these sizes deduced from MIP results are apparent pore sizes and should be interpreted in sense of mercury percolation in pore network. The critical radius r_c is the inflection point on the curve of intruded volume versus pore size, i.e. the pore radius corresponding the peak value in dV/dD curve. According to Katz and Thompson [33], this size corresponds to the smallest pores creating a connected path in pore structure. Moreover, this pore size is found to correlate strongly with the material permeability and ion diffusivity [34]. The median pore radius, based on surface area or intrusion volume estimation, stands for the size value at 50% accumulated surface area (r_m^s) or 50% accumulated intrusion volume (r_m^v). The average pore radius r_a, or mean pore radius, is determined by the ratio between total pore volume and pore surface area. This average value simplifies the real pore structure by a cylindrical tube with r_a as its

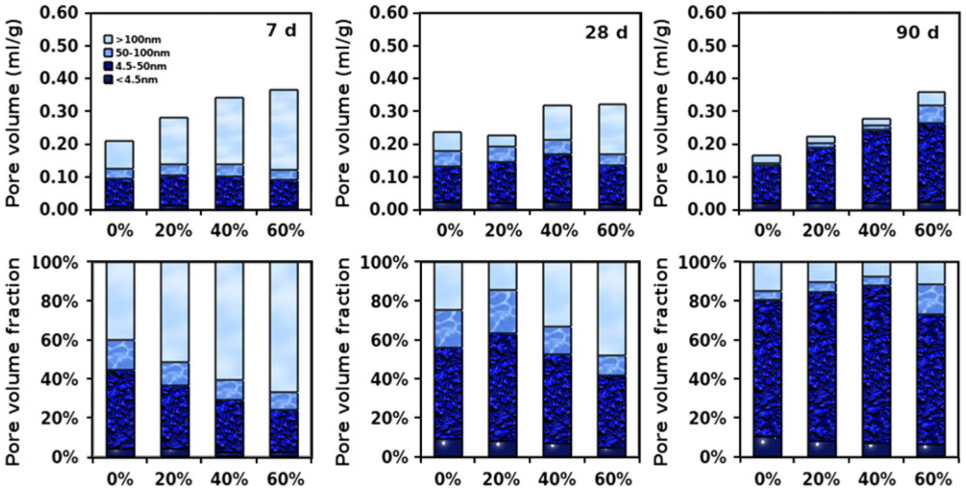

Fig. 3. Pore volume distribution of Paste I (w/b = 0.5) measured by MIP with pore classification from Metha and Monteiro [9].

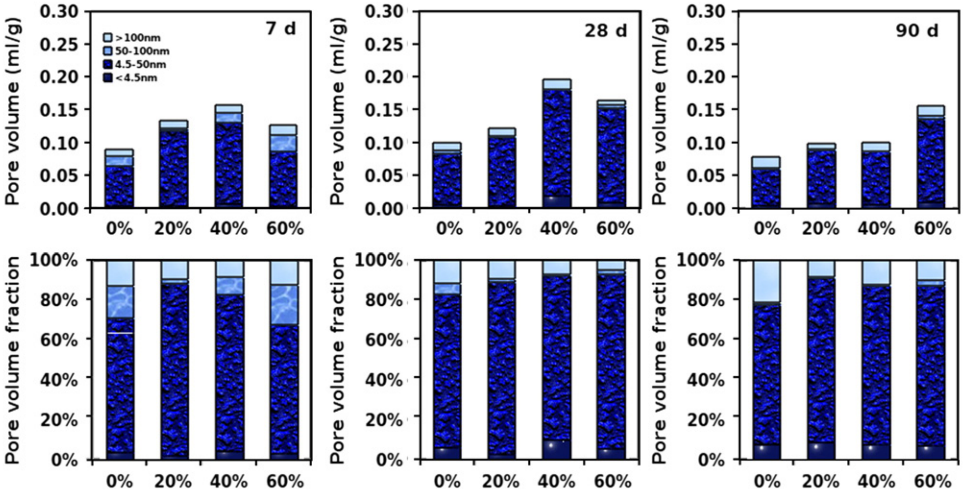

Fig. 4. Pore volume distribution of Paste II (w/b = 0.3) measured by MIP with pore classification of Metha and Monteiro [9].

equivalent radius. All these pore radii are evaluated and presented in Table 5 for all paste samples at different ages.

All characteristic pore sizes of Paste I samples are systematically higher than Paste II. For Paste I, all characteristic pore sizes, except values for r_m^s, decrease with curing age, reflecting in fact the hydrates formation process and the pore filling effect of fly-ash secondary hydration. As for r_m^s, the values are significantly smaller than other sizes due to much larger specific area of porous C–S–H and the values correspond roughly to the dimension of space between C–S–H bundles [39]. That is why this value evolves very little in terms of curing age and fly-ash content. The volume median radius r_m^v reflects the relative importance of capillary pores in whole pore distribution. Consistent with Figs. 3 and 4, the largest r_m^s is due to PIF3 sample with the largest capillary pore fraction. It is interesting to note that r_m^v values are quite near r_c values. Since the C–S–H specific surface dominates and the total intrusion volume does not differ much for samples, the average radius, r_a, gives quite near values for all samples. Moreover, except PIF3 sample, $f_f = 60\%$, all critical pore radii of Paste I samples reach the same level, 10.5 nm at 90 d. For Paste II samples, the correlation between these characteristic sizes with ages and fly-ash contents is less evident although the sizes at 28 and 90 d are generally smaller than 7 d. Again, PIF3 sample, with $f_f = 60\%$ and local w/c = 1.25, shows larger characteristic sizes in all cases.

4. Further analysis

4.1. Hydration degree

The pore structure formation process is related intimately to the hydration kinetics of mineral phases in cement grains and fly-ash particles. Thus the correlation between the hydration degrees of fly-ash cement and the pore structure evolution will be instructive. The hydration degree of cement α_c and the formed gel-space ratio β for fly-ash cement pastes are calculated from the selective dissolution and TGA experiment results as described in Section 2.4. The cement hydration degree is illustrated in Fig. 7 in terms of fly-ash content f_f for different curing ages. It can be seen that the hydration degree is higher for Paste I due to the larger w/b ratio, i.e. more water is available for cement and fly-ash hydration. For Paste II, low porosity, compact pore structure and less available water all limit the hydration extent of minerals in cement grains. As fly-ash is incorporated into cement, the cement is "diluted" with respect to water and fly-ash particles serve as nucleation sites for cement hydration products [3]. By this mechanism, high fly-ash content helps the cement hydration, as indicated in Fig. 7.

Fig. 8 illustrates the total porosity measured by MIP in terms of gel/space ratio β. The total porosity decreases linearly with β for all

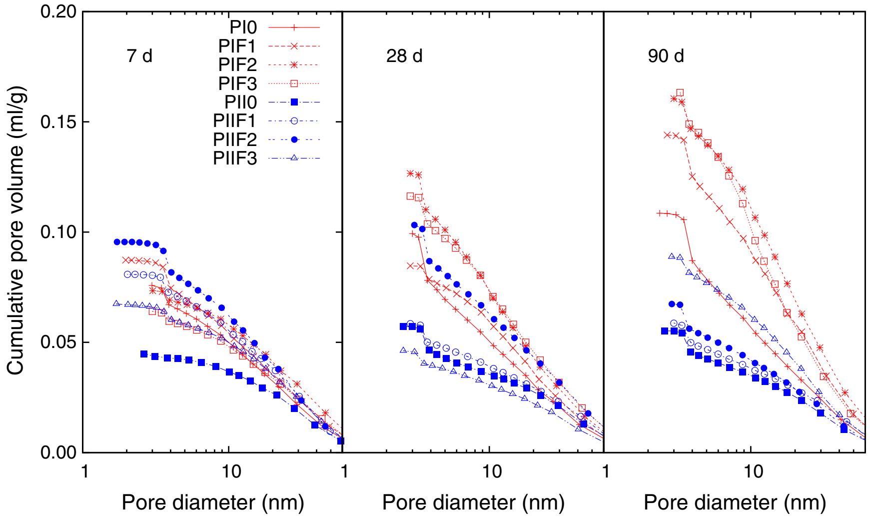

Fig. 5. Cumulative pore volume of fly-ash cement pastes measured by NAD at different ages.

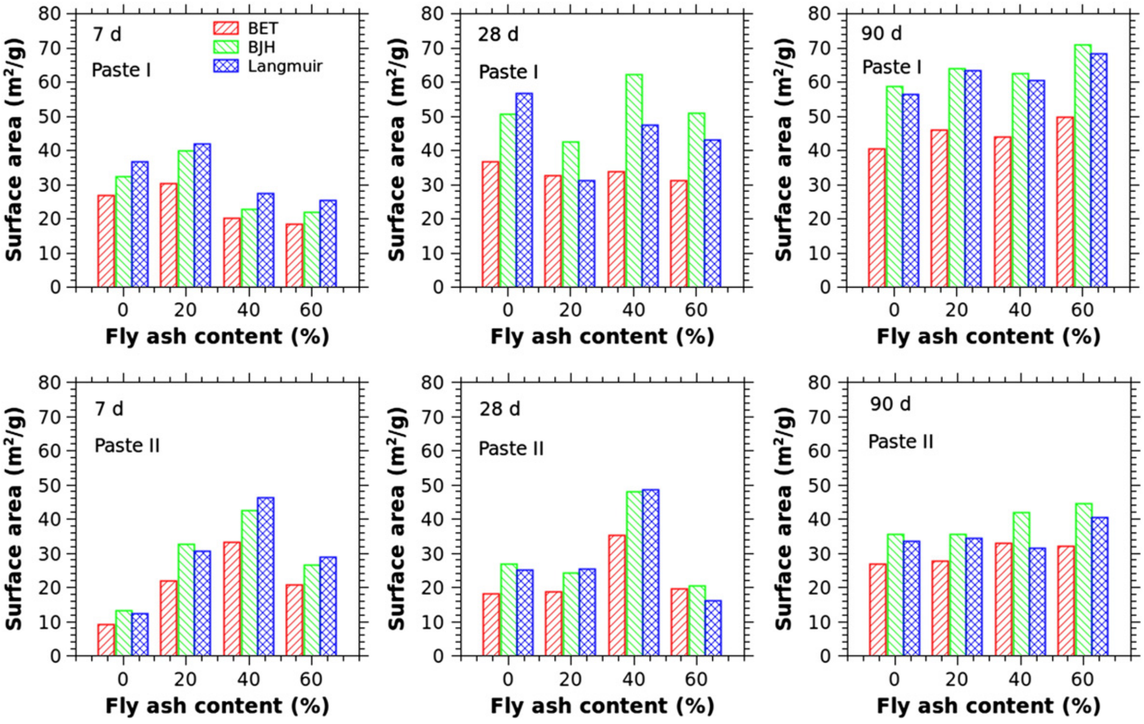

Fig. 6. Surface area of blended pastes at different ages measured by NAD method.

samples. This is not surprising since the C–S–H gel is the main product of hydration and the void space deduced from β is the very definition of porosity. This observation has also been confirmed by Lam et al. [6]. However, the pore volume measured by NAD is found to correlate linearly with cement hydration degree α_c rather than gel/pore ratio β, cf. Fig. 9. The underlying reason lies in the fact that NAD just measures a segment of pore range (micro and meso-pores) and this range is more sensitive to hydration product formation thus to cement hydration degree. Fig. 10 gives BET specific surface area in terms of α_c, showing a clear linear relation. This is because surface area is also dictated by the formation process of hydration products, mechanism proved also by Juenger and Jennings [15].

However, the relation between the critical pore size r_c and the hydration degree or the related gel/space ratio is not evident, cf. Fig. 11. The reason is that the pore structure depends on both how much products are formed and how these products are packed in the space. The hydration degree or gel/space ratio can best capture the former, i.e. the chemical side of pore structure formation, but not the later, i.e. the physical side. That is why on the figure Paste I samples and Paste II samples show so different evolution patterns for r_c in terms of gel/space ratio β. For Paste I samples, the hydration products,

Table 5
Characteristic (apparent) pore radii of fly-ash cement pastes at 7 d, (28 d) and [90 d] measured by MIP.

Samples	Critical radius r_c (nm)	Surface median radius r_m^s (nm)	Volume median radius r_m^v(nm)	Average radius r_a(nm)
PI0	75(38.5)[10.5]	4.25(2.75)[3]	31.2(18.5)[11]	12.7(8.35)[6.25]
PIF1	113(31.2)[10.5]	10.2(3.2)[3.55]	50.3(14.8)[10.9]	19.4(7.25)[6.45]
PIF2	142(60.4)[10.5]	4.3(3.2)[3.9]	80.3(21.5)[10.7]	16.7(8.15)[6.65]
PIF3	277(215)[16.2]	4.3(3.6)[3.7]	112.5(42.2)[12.7]	19.6(10.9)[7.25]
PII0	13.2(13.2)[8.55]	5.4(5.3)[4]	11.8(13.45)[10]	10.2(8.65)[7.1]
PIIF1	13.2(10.5)[13.2]	4.8(3.4)[3.8]	11.8(11)[9.85]	9.2(6.4)[6.5]
PIIF2	13.2(6.1)[8.55]	5.2(3.85)[4.2]	14.2(6.95)[8.05]	8.8(5.3)[5.95]
PIIF3	8.55(6.1)[6.1]	6.7(4.4)[4.45]	13.9(7.8)[6.75]	9.9(6.05)[5.7]

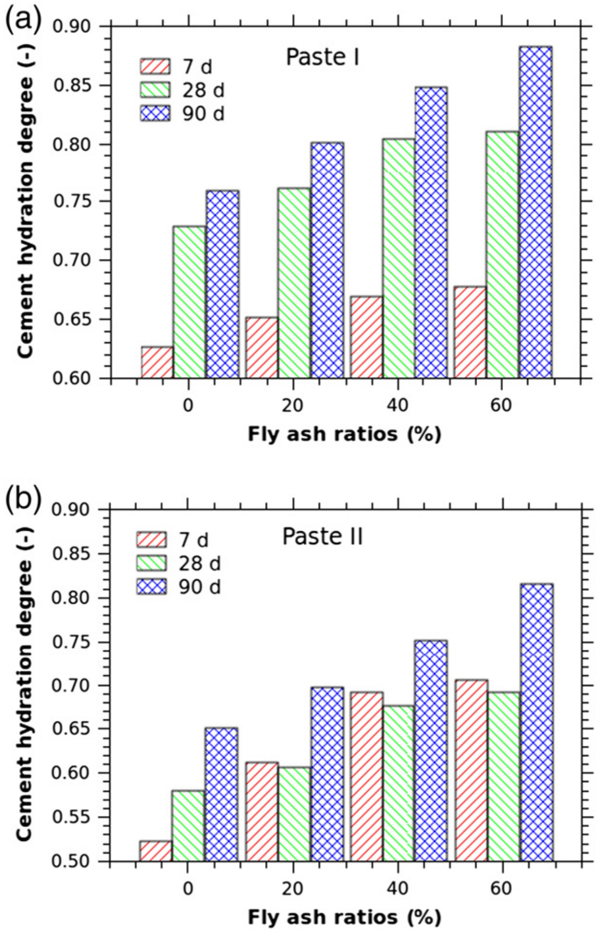

Fig. 7. Hydration degrees of Paste I (a) and Paste II (b) in terms of fly-ash content at ages of 7 d, 28 d and 90 d.

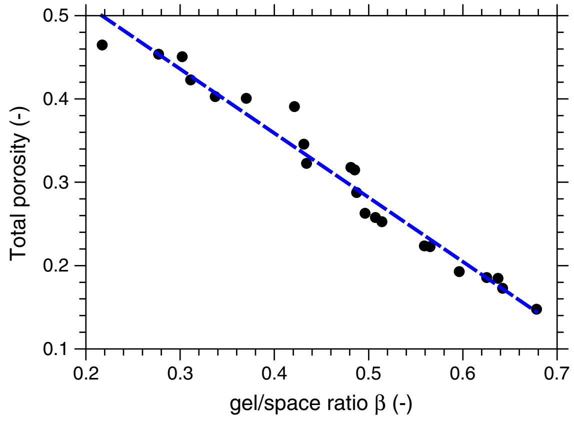

Fig. 8. Total MIP porosity in terms of gel/space ratio.

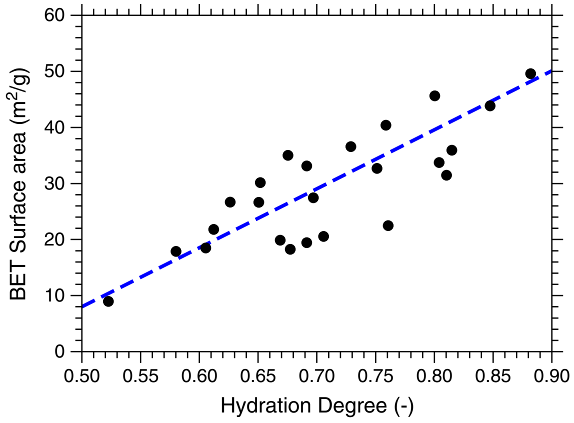

Fig. 10. BET surface area in terms of cement hydration degree.

along with new product formation, continue to change the space packing patterns from 7 d to 90 d while the product packing is relatively fixed ever since 7 d for Paste II samples. Finally all samples for paste II adopt r_c at same magnitude, 6–16 nm.

4.2. Fly-ash contribution

The pore structure characteristics are compared between the fly-ash cement pastes (PI1–3, PII1–3) and pure cement pastes (PI0, PII0). We define the relative porosity φ/φ_0, relative BET surface area S/S_0, relative critical pore size r_c/r_{c0} and relative pore volume with size smaller than 50 nm α/α_0. The subscript “0” represents pure cement pastes. Note that the pore size of 50 nm is of particular interest since from this size the pores are assumed to be detrimental from durability consideration for cementitious composites [9].

Fig. 12 shows all these relative values in terms of fly-ash content f_f. It is observed that the relative porosity φ/φ_0 increases with fly-ash content independent of the w/b ratios and Paste II samples (w/b = 0.3) are more sensitive to fly-ash content. For the parameter α/α_0, the fly-ash content decreases the pore fraction for Paste I but has no clear influence on Paste II, and this difference converges with the curing age. For S/S_0, the fly-ash content tends to augment the relative surface for Paste II (w/b = 0.3) but not for Paste I (w/b = 0.5). For r_c/r_{c0}, the fly-ash content seems to increase the relative critical sizes for Paste I (w/b = 0.5) but to decrease this value for Paste II (w/b = 0.3), and the difference vanishes as curing age attains 90 d. If all values are compared at age of 90 d, the PIF3 sample (w/b = 0.5, $f_f = 60\%$) again shows its particularity in terms of α/α_0 and r_c/r_{c0} due to its large local w/c ratio (w/c = 1.25).

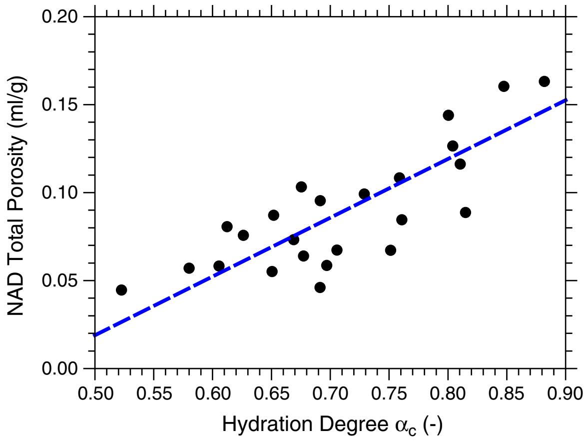

Fig. 9. Total NAD pore volume in terms of cement hydration degree.

All these observations are related to the double effects of incorporating fly-ash into pure Portland cement. Physically, the fly-ash serves as nucleation sites for the cement hydration products thus helps to achieve a higher hydration level for cement grains. On chemical side, fly-ash particles undergo themselves the hydration process (pozzolanic reaction), much later compared to cement hydration, with water and $Ca(OH)_2$, one of the hydration products from cement. The product of fly-ash hydration fills the already formed pore structure and a global refinement of pore distribution can be thus achieved. But this mechanism holds for local w/c of pastes controlled to a certain value, e.g. local w/c ≈ 1.0 in this study. Too large local w/c, e.g. PIF3 with local w/c = 1.25, will cancel the pore refinement effect of fly-ash hydration.

Take r_c/r_{c0} for example. Paste I samples contain more water thus the residual free water from cement hydration leaves coarser pores, these pores are refined progressively with the fly-ash hydration, but this process fails for PIF3 sample. Paste II samples contain much less water and the hydration products pack into a dense pore structure, moreover further hydration of cement and fly-ash is much limited due to the very rare unreacted free water, thus the critical pore size does not evolve much with curing age.

4.3. DPSD from MIP and NAD

The differential pore size distributions (DPSD) measured by MIP and NAD for all samples at 7 d, 28 d and 90 d are presented in Figs. 13, 14 and 15 respectively. The reflection points on the MIP curves correspond to the critical pore sizes. It is recalled that all pore sizes refer to the percolation sizes of pores in an interconnected structure.

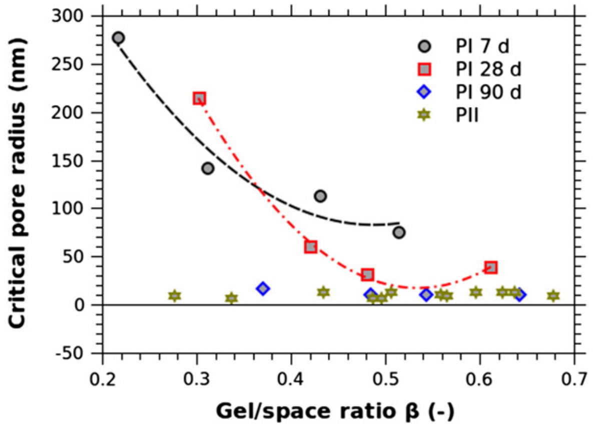

Fig. 11. Critical pore radii measured by MIP in terms of gel/space ratio.

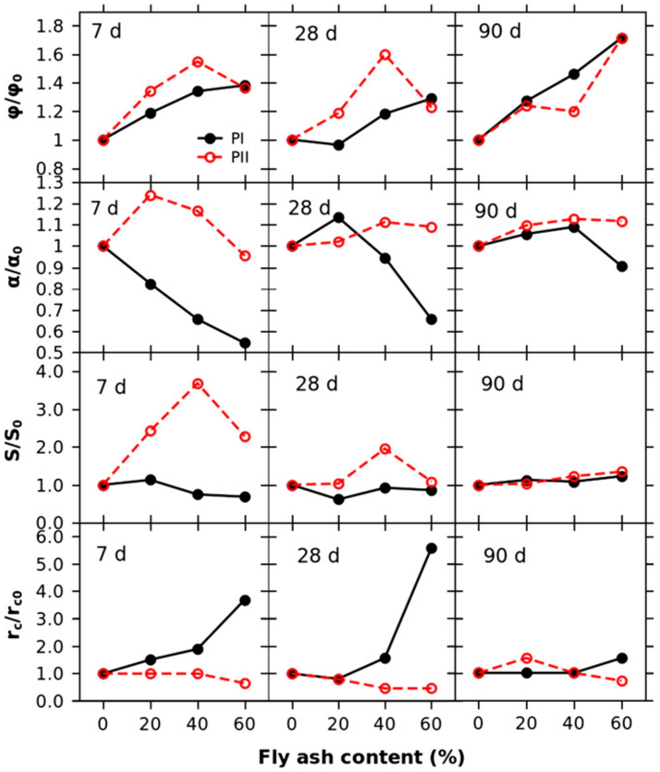

Fig. 12. Influence of fly-ash content on the relative porosity φ/φ_0, relative pore volume (<50 nm) α/α_0, relative BET surface area S/S_0 and relative critical pore radius r_c/r_{c0} (filled circles for PI samples, void circles for PII samples).

The comparison between NAD and MIP curves give several important observations. The first is that the DPSP from MIP is systematically higher than that from NAD, especially at critical pore size this difference attains its maximum. The two curves remain consistent for the pore size range of 2–20 nm. Actually, two basic mechanisms contribute to the DPSP difference. Firstly, the application pore range for NAD measurement is within 60 nm due to the pore condensation condition of nitrogen, in other words, NAD cannot capture the pore near or greater than this limit [26]. The other mechanism is the inherent difference between the pore volume estimations by mercury filling process (MIP intrusion phase) and by nitrogen desorption process (NAD desorption phase) although the two processes are assumed equivalent in point view of non-wetting phase invasion [17]. If "ink-bottle" pores exist in the pore structure, for MIP measurement, the pore volume includes both the neck (smaller radius) and the bottle (larger radius) if the applied pressure is enough to penetrate the neck. And the penetrated neck size, instead of bottle size, accounts for the intruded volume. During nitrogen desorption, as the neck is in desorption the involved pore volume is just the neck volume as the bottle pore size is usually greater than the condensation limit.

The second observation is that NAD curves show two typical peaks at $d = 3.5$ nm (Peak I) and $d \sim 20$ m (Peak II). Furthermore, the pore size for Peak I remains almost constant for all samples at all ages while the pore size for Peak II seems to adopt larger value for Paste I (w/b = 0.5) than for Paste II (w/b = 0.3). For Peak I, the corresponding pore size agrees well with the interlayer pore size of hydration product C–S–H, and this peak is due to the gel (interlayer) pore condensation of nitrogen. The same conclusion is also reached by other authors [36,37]. The Peak II has a similar physical meaning as the inflection point in DPSD of MIP, and it represents the smallest pore size under which the pore condensation is no more percolated.

Thirdly, the DPSDs from NAD for Paste I (w/b = 0.5) samples are systematically higher than those of Paste II (w/b = 0.3) samples. Besides the aforementioned mechanism of more advanced hydration under high w/b ratio, the different structures of formed C–S–H hydrates are also important. According to relevant research [38,39], two types of C–S–H hydrates exist: low density (LD) and high density (HD). The LD C–S–H, having a more porous structure and partially accessible to nitrogen, is more likely to form under high water availability (high w/b) while the HD C–S–H, having more compact structure and not accessible to nitrogen, is to form under low water availability (low w/b) [35,40]. Moreover, with hydration process the LD C–S–H can progressively change into HD C–S–H [41,42]. That explains the DPSD evolution for both w/b cases.

5. Conclusion

1. The pore structure of fly-ash cement pastes can be described by pore size distribution, total porosity, pore specific surface area as well as some characteristic pore sizes. The pore structure is the result of the related hydration processes of cement and fly-ash. Both chemical reaction kinetics and physical packing of hydrates count

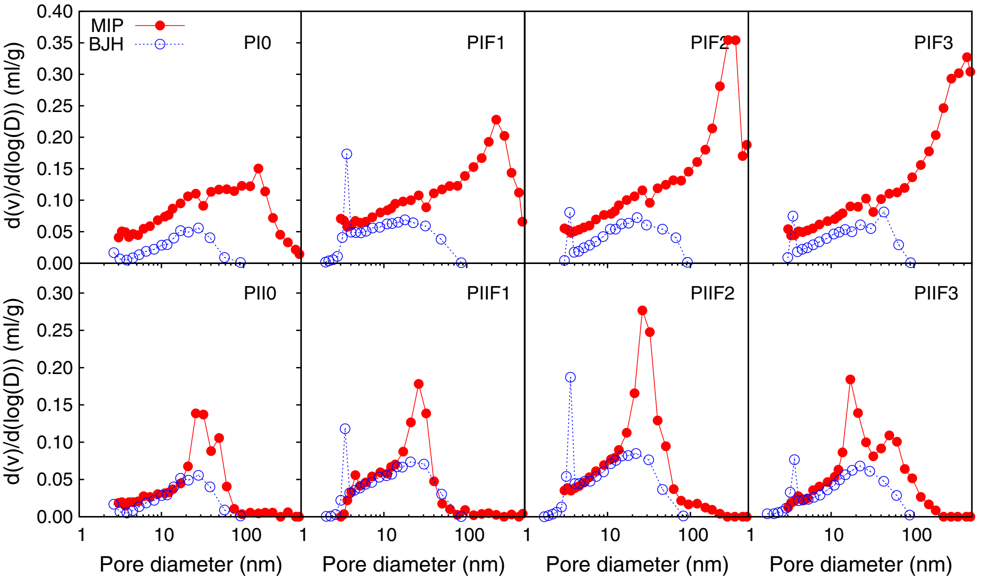

Fig. 13. DPSD of fly-ash cement pastes at age of 7 d (filled circles for MIP data, void circles for NAD data).

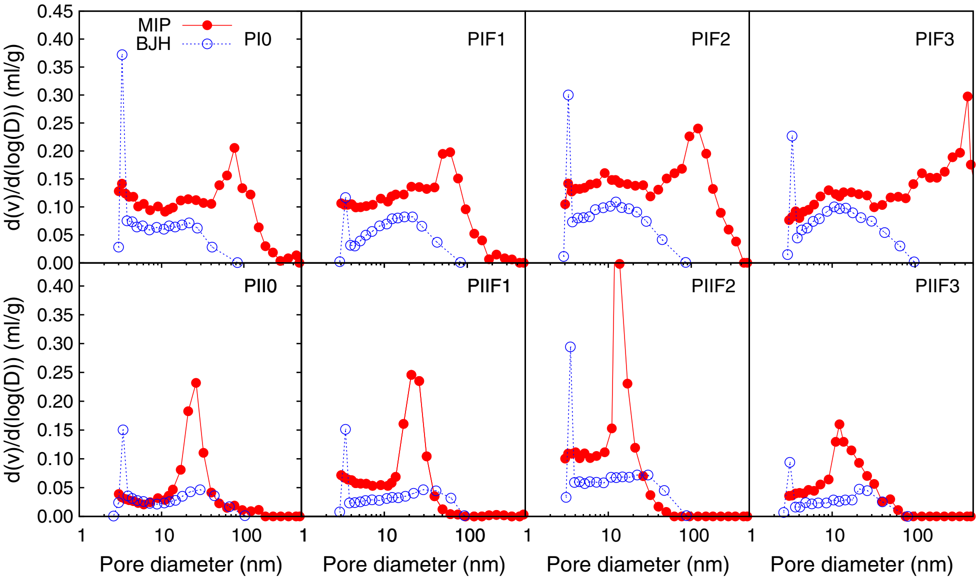

Fig. 14. DPSD of fly-ash cement pastes at age of 28 (filled circles for MIP data, void circles for NAD data).

for the pore structure. The hydration kinetics is quantified by cement hydration degree and the formed gel/space ratio. Among the pore structure characteristics, the total porosity (NAD) and specific surface area are found to correlate linearly with the cement hydration degree while the pore size distribution, with its characteristic pore sizes, shows no correlation with the chemical kinetics but related more to hydration product packing pattern. The packing pattern is much governed by the macroscopic parameter of water to binder ratio.

2. As fly-ash is blended to cement, fly-ash plays double roles during the hydration and pore structure formation processes. The physical role is to provide more nucleation sites for the precipitation of cement hydration products thus accelerate the hydration process of cement. Later on, the hydration of fly-ash forms products and fills the already formed pore structure. These two mechanisms are clearly observed for Paste I samples with w/b = 0.5. However, the second mechanism is much less important as the w/b is decreased, as for Paste II with w/b = 0.3. Under this situation, the packing of cement hydrates reaches a very dense degree with limited hydration degree of cement grains and later the secondary hydration of fly-ash fills further the available pore space but always to a limited extent. Thus, a dense pore structure can be achieved at early age and the total porosity can evolve with the hydration and secondary hydration, but the relative distribution of pore ranges, as well as the critical pore size, remains basically the same. It is also observed that the filling effect of fly-ash hydration can be mobilized only as the local w/c ratio of fly-ash pastes is controlled to a certain level, around w/c = 1.0 in this study.
3. Different experimental methods for pore structure evaluation are also used and compared in this study. For total porosity evaluation, the pretreatment by oven-drying at 105 °C is the most efficient way to dry the samples while solvent exchange by methanol shows also a reliable pretreatment method for gravimetry measurement. For specific area measurement, the Langmuir and BET estimations give bound values for real surface areas while the BJH interpretation for NAD experiment tends to overestimate the

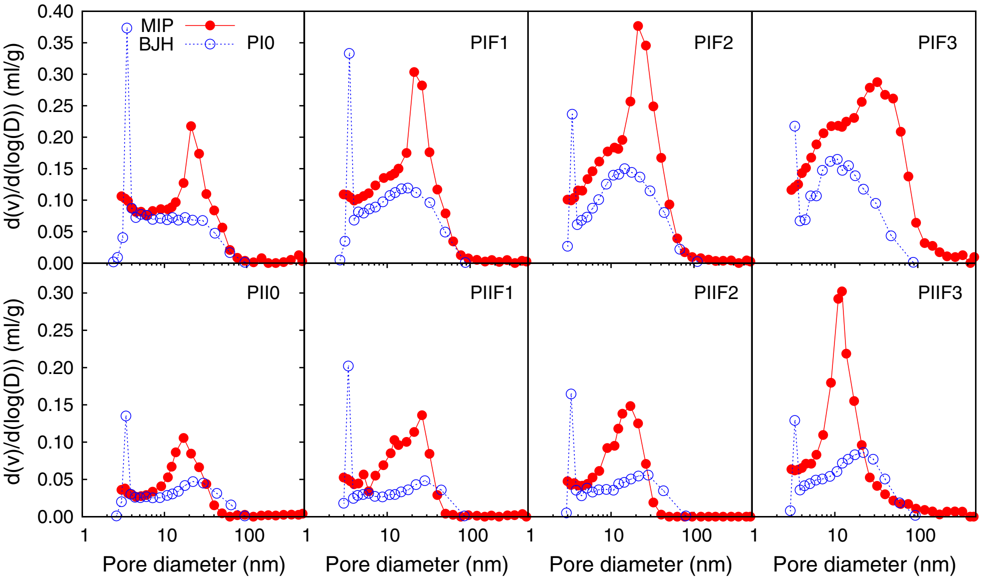

Fig. 15. DPSD of fly-ash cement pastes at age of 90 d (filled circles for MIP data, void circles for NAD data).

surface area as “ink-bottle” pores exist. For pore size distribution measurement, MIP results should be interpreted in pore percolation sense. For micropore and meso-pore ranges, 2–20 nm, the NAD measurement affords more detailed information on the interlayer pores of C–S–H hydrates (gel). From this study, this characteristic pore size at this level is found to be about 3.5 nm.

Acknowledgment

The research is supported by China national major fundamental research grant (973 Program, no. 2009CB623106).

References

[1] P.K. Metha, High-performance, high-volume fly ash concrete for sustainable development, Proceedings of the International Workshop on Sustainable Development and Concrete Technology, Beijing, 2004, pp. 3–14.

[2] P.C. Aitcin, High Performance Concrete, E& FN SPON, London, 1998.

[3] M. Cyr, P. Lawrence, E. Ringot, Efficiency of mineral admixtures in mortars: quantification of the physical and chemical effects of fine admixtures in relation with compressive strength, Cem. Concr. Res. 36 (2006) 264–277.

[4] A. Xu, S.L. Sakar, L.O. Nilsson, Effect of fly ash on the micro-structure of cement mortar, Mater. Struct. 26 (1993) 414–424.

[5] R.F. Feldman, H. Cheng-Yi, Microstructure properties of blended cement mortars and their relation to durability, Proceedings of the RILEM Seminar on Durability of Concrete Structures under Normal Outdoor Exposure, Hannover, March, 1984, pp. 133–140.

[6] L. Lam, Y.L. Wong, C.S. Poon, Degree of hydration and gel/space ratio of high-volume fly ash/cement systems, Cem. Concr. Res. 30 (2000) 747–756.

[7] V.G. Papadakis, Effect of fly ash on Portland cement systems Part I. Low-calcium fly ash, Cem. Concr. Res. 29 (1999) 1727–1736.

[8] E.E. Berrey, R.T. Hemmings, B.J. Cornelius, Mechanisms of hydration reaction in high volume fly ash cements and mortars, Cem. Concr. Compos. 12 (1990) 253–261.

[9] P.K. Metha, P.J.M. Monterio, Concrete, Microstructure, Properties and Materials, McGraw-Hill, London, 2006.

[10] S. Diamond, Mercury porosimetry: an inappropriate method for the measurement of pore size distributions in cement-based materials, Cem. Concr. Res. 30 (2000) 1517–1525.

[11] C.A. Léony Léon, New perspectives in mercury porosimetry, Adv. Colloid Interface Sci. 76–77 (1998) 341–372.

[12] G. Helbet, Mercury porosimetry: a general (practical) overview, Part. Part. Syst. Charact. 23 (2006) 9–19.

[13] E.P. Barrett, L.G. Joyner, P.P. Halenda, The determination of pore volume and area distributions in porous substances. I. Computations from nitrogen isotherms, J. Am. Chem. Soc. 73 (1951) 373–380.

[14] T.C. Powers, T.L. Brownyard, Studies of the physical properties of hardened portland cement paste, ACI J. Proc. 43 (1947) 845–880.

[15] M.C.G. Juenger, H.M. Jennings, The use of nitrogen adsorption to assess the microstructure of cement paste, Cem. Concr. Res. 31 (2001) 883–892.

[16] R.S. Mikhail, E. Copeland, S. Brunauer, Pore structure and surface areas of hardened Portland cement pastes by nitrogen adsorption, Can. J. Chem. 42 (1964) 426–438.

[17] S.P. Rigby, R.S. Fletcher, S.N. Riley, Characterisation of porous solids using integrated nitrogen sorption and mercury porosimetry, Chem. Eng. Sci. 59 (2004) 41–51.

[18] J. Echeverria, M.T. Morera, C. Mazkiarán, J.J. Garrido, Characterization of the porous structure of soils: adsorption of nitrogen (77 K) and carbon dioxide (273 K), and mercury porosimetry, Eur. J. Soil Sci. 50 (1999) 497–503.

[19] M. Hartmann, A. Vinu, Mechanical stability and porosity analysis of large-pore SBA-15 mesoporous molecular sieves by mercury porosimetry and organics adsorption, Langmuir 18 (2002) 8010–8016.

[20] J. Kaufmann, R. Loser, A. Leeman, Analysis of cement-based materials by multi-cycle mercury intrusion and nitrogen sorption, J. Colloid Interface Sci. 336 (2009) 730–737.

[21] J. Kaufmann, Pore space analysis of cement-based materials by combined Nitrogen sorption–Wood's metal impregnation and multi-cycle mercury intrusion, Cem. Concr. Compos. 32 (2010) 514–522.

[22] R.H. Bogue, Calculation of the compounds in Portland cement, Ind. Eng. Chem. 1 (1929) 192–197.

[23] J.J. Beaudoin, B. Tamtsia, J. Marchand, H.R. Myers, Solvent exchange in partially saturated and saturated microporous systems: length change anomalies, Cem. Concr. Res. 30 (2000) 359–370.

[24] N.C. Collier, J.H. Sharp, N.B. Milstone, J. Hill, I.H. Godfrey, The influence of water removal techniques on the composition and microstructure of hardened cement pastes, Cem. Concr. Res. 38 (2008) 737–744.

[25] E.W. Washburn, Note on a method of determining the distribution of pore sizes in a porous material, PNAS 7 (1921) 115–116.

[26] K.K. Aligizaki, Pore Structure of Cement-based Materials—Testing, Interpretation and Requirement, Taylor & Francis, New York, 2006.

[27] R.P. Rigby, R.S. Fletcher, J.H. Raistrick, S.N. Riley, Characterization of porous solids using a synergistic combination of nitrogen sorption, mercury porosimetry, electron microscopy and micro-focus X-ray imaging techniques, Phys. Chem. Chem. Phys. 4 (2002) 3467–3481.

[28] H.F.W. Taylor, Cement Chemistry, second ed. Thomas Telford, London, 1997.

[29] M.B. Haha, K.D. Weerdt, B. Lothenbach, Quantification of the degree of reaction of fly ash, Cem. Concr. Res. 40 (2010) 1620–1629.

[30] J.I. Escalante-Garcia, Nonevaporable water from neat OPC and replacement materials in composite cements hydrated at different temperatures, Cem. Concr. Res. 33 (2003) 1883–1888.

[31] R.F. Feldman, Diffusion measurements in cement paste by water replacement using propan-2-ol, Cem. Concr. Res. 17 (4) (1987) 602–612.

[32] E. Robens, B. Benzler, G. Buchel, H. Reichert, K. Schumacher, Investigation of characterizing methods for the microstructure of cement, Cem. Concr. Res. 32 (2002) 87–90.

[33] A.Z. Katz, A.J. Thompson, Quantitative prediction of permeability in porous rock, Phys. Rev. B 34 (1985) 8179–8185.

[34] P. Halamickova, R.J. Detwiler, D.P. Bentz, E.J. Garboczi, Water permeability and chloride ion diffusion in Portland cement mortars: relationship to sand content and critical pore diameter, Cem. Concr. Res. 25 (1995) 790–802.

[35] H.M. Jennings, A model for the microstructure of calcium silicate hydrate in cement paste, Cem. Concr. Res. 30 (2000) 101–116.

[36] A.J. Allen, J.J. Thomas, H.M. Jennings, Composition and density of nanoscale calcium–silicate–hydrate in cement, Nat. Mater. 6 (2007) 311–316.

[37] T.C. Powers, Structure and physical properties of hardened Portland cement paste, J. Am. Ceram. Soc. 41 (1958) 1–6.

[38] J.J. Thomas, A.J. Allen, H.M. Jennings, Structural changes to the calcium–silicate–hydrate gel phase of hydrated cement with age, drying, and resaturation, J. Am. Ceram. Soc. 91 (2008) 3362–3369.

[39] H.M. Jennings, Refinements to colloid model of C–S–H in cement: CM-II, Cem. Concr. Res. 38 (2008) 275–289.

[40] P.T. Tennis, H.M. Jennings, A model for two types of calcium silicate hydrate in the microstructure of Portland cement pastes, Cem. Concr. Res. 30 (2000) 855–863.

[41] G. Constantinides, F.-J. Ulm, The nanogranular nature of C–S–H, J. Mech. Phys. Solids 55 (2007) 64–90.

[42] F.-J. Ulm, G. Constantinides, F.H. Heukamp, Is concrete a poromechanics material? A multiscale investigation of poroelastic properties, Mater. Struct. 37 (2004) 43–58.